engineering proceedings

MDPI

Proceeding Paper

Scaling the Response of a Simplified Hull Girder Subjected to Underwater Explosions †

Giovanni Marchesi *, Luca Lomazzi, Marco Giglio and Andrea Manes

Politecnico di Milano, Department of Mechanical Engineering, Via La Masa n.1, 20156 Milan, Italy; luca.lomazzi@polimi.it (L.L.); marco.giglio@polimi.it (M.G.); andrea.manes@polimi.it (A.M.)

* Correspondence: giovanni.marchesi@polimi.it

† Presented at the 53rd Conference of the Italian Scientific Society of Mechanical Engineering Design (AIAS 2024), Naples, Italy, 4–7 September 2024.

Abstract: Underwater explosions (UNDEXs) represent a significant threat to marine vessels, motivating the analysis of their resulting dynamic response and damage. Conducting experimental investigations on full-scale ships, while being the most consistent strategy, is not always feasible due to obvious economic constraints. Consequently, researchers usually rely on scaled models designed to replicate real-world scenarios in laboratory environments. Despite the widespread use of this approach, the scaling laws between prototypes and models are not yet satisfactory due to the complexity of the UNDEX phenomena and the variability in boundary conditions. To address this aspect, the present study focuses on the scalability of a simplified vessel, termed a simplified hull girder (SHG). This study is conducted numerically and originates from a comparison with experiments available in the literature. This work has two objectives: firstly, it provides a practical approach to simulating the behaviour of complex architectures that undergo severe deformation due to blast loads, a critical challenge for state-of-the-art computational methods. Secondly, this work aims to assess the reliability of the scaling laws commonly used in UNDEX scenarios and to highlight the importance of strain-rate effects.

Keywords: scaling; underwater explosions; simplified hull girder; dimensional analysis; numerical modelling

Academic Editors: Umberto Galietti, Gabriele Arcidiacono, Enrico Armentani, Davide Castagnetti, Vigilio Fontanari, Aurelio Somà and Nicola Bonora

Published: 19 February 2025

Citation: Marchesi, G.; Lomazzi, L.; Giglio, M.; Manes, A. Scaling the Response of a Simplified Hull Girder Subjected to Underwater Explosions. *Eng. Proc.* **2025**, *85*, 19. https://doi.org/10.3390/engproc2025085019

1. Introduction

Studying the response of naval platforms subjected to the effects of an underwater explosion (UNDEX) is a challenging task, especially from an experimental perspective. The combination of the size of the structures involved and the critical nature of the loading conditions makes experimental campaigns expensive. Hence, tests are typically conducted using scaled models. This shifts the challenge towards identifying the relationship between the prototype and the scaled model. The latter must, apart from the scaling factors, confidently replicate the behaviour of the prototype. Otherwise, the experimental data are not representative. The first attempts to introduce scaling laws date back to Cole [1] and focused solely on the effects of underwater explosions, without covering the structural response. More recently, attention has shifted towards the search for comprehensive scaling laws that take into account the multi-physical nature of UNDEX scenarios, addressing both the structural and dynamic fluid nature of the phenomena. Scaled models are generally defined based on representative dimensionless numbers. They can be identified either by obtaining the governing equations in dimensionless form or by performing a dimensional analysis. The latter strategy is more general as the equations are not necessary, even though

it requires full knowledge of all the variables governing the scenario under investigation. Nonetheless, while scaling laws for explosions in air have been widely studied in the literature, especially for blast-loaded plates [2–4], in the marine environment, the problem has only been partially addressed. Among the few works on the topic, two are worth mentioning. By leveraging dimensional analysis, Yao et al. [5] proposed a new impact factor for developing scaled models of naval platforms and validated the approach with several case studies. Huang et al. [6,7] identified a dimensionless group to describe and scale the response of dams subjected to underwater explosions. The primary reason why the progress of the literature on UNDEXs does not match that of explosions in air is due to the physics of the phenomena involved. It is well known that an underwater explosion generates an additional effect beyond the primary shock. This additional effect is the gas bubble caused by the formation of gaseous detonation products within a denser liquid, i.e., water, which confines its movement. Defining a scaling law that accounts for both phenomena, as already noted by Cole [1], requires gravity modulation. This procedure is feasible for fully constrained structures, where centrifugal similarity [8] can be applied, enabling centrifuge testing on plates and dams. For floating platforms, however, centrifuge testing is evidently much more complex, and thus gravity must be treated as an invariant. As a result, it becomes impossible to define a law able to scale both primary shock and bubble effects simultaneously.

In this work, the established procedure of dimensional analysis was used to verify the feasibility of scaling the response of a simple naval platform. Specifically, a simplified hull girder (SHG) was considered, a structure commonly found in the literature [9–12] due to, firstly, its ease of construction and, secondly, its ability to reasonably replicate the global behaviour of more complex naval platforms [13]. The scalability of an SHG was investigated numerically, leveraging coupled Eulerian–Lagrangian (CEL) analyses. The modelled setup, i.e., the prototype, corresponds to a precise scenario studied experimentally by Zhang et al. [14], and the available data were used for validation. In the experimental scenario, the effects of the gas bubble were assumed to be negligible compared to those induced by the shock. The results obtained are thus conceptually extendable to scenarios similar to the one discussed or others where the gas bubble does not interact with the naval platform. Moreover, strain rate effects were ignored while defining the scaled models to align with the work of Yao et al. [5], in which a similar SHG prototype was successfully scaled without accounting for strain-rate effects. The primary goal was thus to assess whether laboratory models of SHGs can be defined based solely on geometric–static considerations. This strategy is rejected in some of the aforementioned studies [6,7] in which dissimilar effects induced by strain rate hindered the development of scaled models. Additionally, the experimental data enable a comparison of the temporal evolution of the structural response, which is different from similar works. The deformed configuration of the structure was usually considered only at a given time instant.

The novelty of this work also lies in the procedure developed to improve the accuracy of the simulations. In fact, artificial structural elements are introduced to enforce the connection between the Eulerian and Lagrangian mesh and overcome the inherent limitations of traditional coupling algorithms. The properties of the artificial elements are properly modulated to avoid altering the structural response and to ensure satisfactory results when compared with experiments.

2. Materials and Methods

This section is organised into three subsections. The first describes the case study and presents the simplified hull girder, the second delves into the numerical modelling procedure, and the third describes the dimensional analysis employed to scale the naval platform.

2.1. Case Study: Simplified Hull Girder

The simplified hull girder considered in this work was experimentally studied by Zhang et al. [14]. This configuration was specifically chosen by the authors since the time history of the central point was measured experimentally. The main information on the tested setup is briefly reported hereafter. An isometric view is shown in Figure 1, while Figure 2 illustrates the main dimensions of the system. The structure has a length of 2.5 m, a height of 0.12 m, and a width of 0.3 m. It is composed of 9 cabins, each with a longitudinal extent of 0.278 m. The upper deck features an opening for each cabin, resulting in stringers with extents of 20 mm (l_p) and 70 mm (b_p), as shown in Figure 2. The structure is made of mild steel and has a uniform thickness of 3 mm (h_p). The draught corresponds to half of the height, i.e., 0.06 m. The SHG was subjected experimentally to the effects of a 55 g TNT charge located under the midship at a stand-off distance of 0.2 m. It results in a scaled distance $(Z = R/W^{1/3})$ of 0.52 m/kg$^{1/3}$. The underwater explosion induces local deformation of the central plate, whose behaviour can be assimilated to that of a plate with flexible supports at its extremities. Moving away from the centre, the lower panels experience progressively decreasing deformations. All other structural elements essentially behave rigidly. The local response governs the global behaviour of the structure, resulting in a combination of hogging and rigid-body motion. Figure 3 shows a qualitative deformed shape of the structure, highlighting the central plastic hinge and the rigid motion. To understand whether the gas bubble formed by the UNDEX contributes to the structural response, one can rely on the empirical formulas available in Ref. [1] and compute the maximum radius and the pulsation period of the bubble assuming its free motion. The former quantity is approximately 0.6 m, larger than the stand-off distance, and the latter is almost 113 ms, longer than the time associated with the hog distortion transient. These results, combined with the experimental evidence, demonstrate that the effects of the gas bubble are negligible compared to the primary shock. In fact, a deformed shape close to the permanent configuration is reached before the secondary effects of the bubble can manifest. This result was a necessary condition for applying the scaling procedure described in the present work, and similar considerations were adopted in Ref. [15] to create scale models for dams.

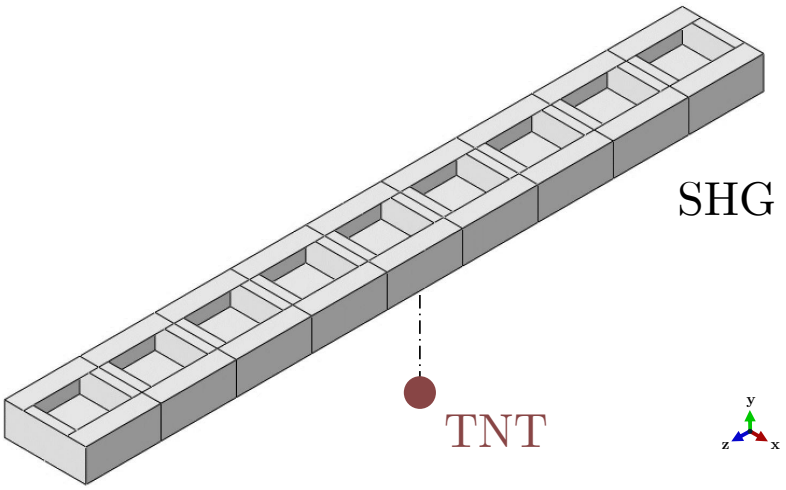

Figure 1. Axonometric view of a simplified hull girder prototype.

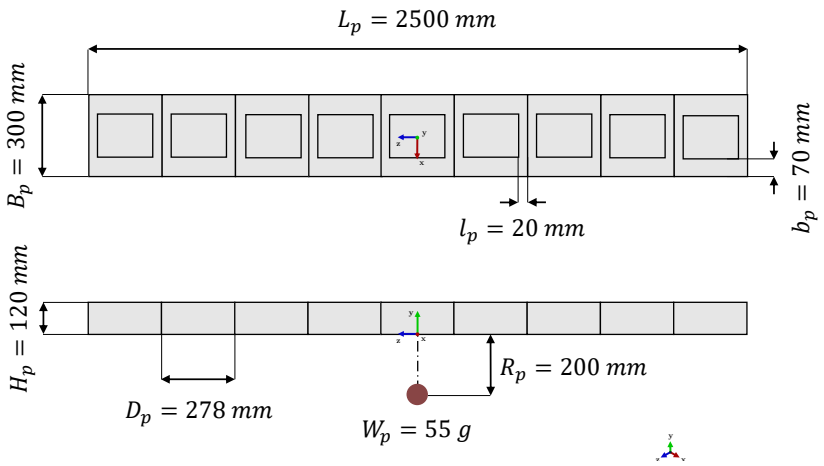

Figure 2. General dimensions of a simplified hull girder prototype. Setup taken from Ref. [14].

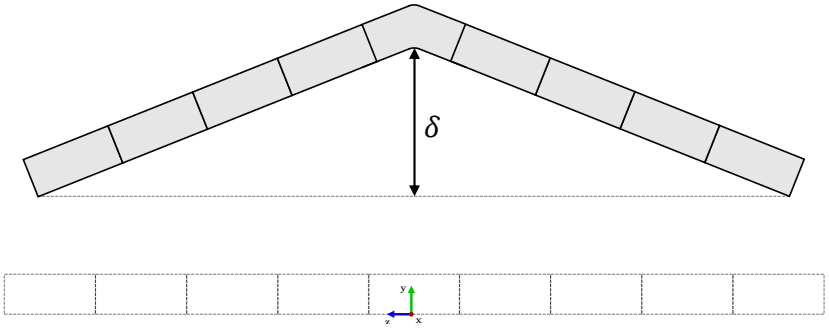

Figure 3. Qualitative deformed shape overlapping the undeformed configuration and the identification of hog distortion.

2.2. Numerical Modelling

This section addresses the numerical modelling procedure for the SHG in Figure 2 and the associated small-scale models. The prototype and the scaled models were investigated numerically through coupled Eulerian–Lagrangian analyses. Hence, the fluid part, i.e., the dynamics of the underwater explosion, was analysed using the Eulerian solver, while the structural part, i.e., the SHG, was described using the Lagrangian solver. Fluid–structure interaction (FSI) was modelled through a coupling algorithm. This required the definition of a coupling surface that acts as a boundary to the flow of material in the Eulerian mesh, while the stresses in the Eulerian material exert forces on the surface, distorting the Lagrangian mesh. The Eulerian mesh was analysed through a multi-material solver, in which water was modelled according to a polynomial equation of state (Equation (1)), including only the bulk modulus ($a_1 = 2200$ MPa, $\rho_{0,w} = 1000\ \mathrm{kg/m^3}$) and imposing a zero cut-off pressure. This latter condition handles cavitation, preventing regions of nonphysical negative pressure. The TNT explosive was described by the Jones–Wilkins–Lee (JWL) equation of state (Equation (2)) [16], with the parameters taken from Ref. [17] and listed in Table 1. The JWL equation of state (EOS) is the most commonly adopted model to describe the adiabatic expansion of detonation products. Its parameters are empirical and calibrated experimentally for different types of explosives. The last term in the equation corresponds to the EOS of ideal gases, while the two exponential terms are introduced to ensure its validity across a wider pressure range. A detailed explanation of how to determine the empirical parameters can be found in Ref. [16]. The detonation is initiated at the charge centre and proceeds at a constant velocity (6930 m/s). Finally, air was modelled as an

ideal gas (Equation (3)) with constant $\gamma = 1.4$. The subscripts w, TNT, and a were added in Equations (1)–(3) to explicitly refer to water, explosive, and air, respectively.

$$p_w = a_1 \left(\frac{\rho_w}{\rho_{0,w}} - 1 \right) \tag{1}$$

$$p_{TNT} = p_0 + A_1 \left(1 - \frac{\omega \rho_{TNT}}{R_1 \rho_{0,TNT}} \right) e_{TNT}^{-\frac{R_1 \rho_{0,TNT}}{\rho_{TNT}}} + A_2 \left(1 - \frac{\omega \rho_{TNT}}{R_2 \rho_{0,TNT}} \right) e^{-\frac{R_2 \rho_{0,TNT}}{\rho_{TNT}}} + \omega \rho_{TNT} e_{TNT} \tag{2}$$

$$p_a = (\gamma - 1) \rho_a e_a \tag{3}$$

Table 1. JWL equation of state parameters for TNT [17].

$\rho_{0,TNT}$ (kg/m^3)	p_0 (MPa)	A_1 (GPa)	A_2 (GPa)	R_1 (-)	R_2 (-)	ω (-)
1630	≈0.1	374	37.3	4.15	0.95	0.35

The mild steel of the SHG was modelled with elastic, perfectly plastic behaviour, having a static yield strength (σ_0) of 250 MPa, a density of 7850 kg/m^3, an elastic modulus of 210 GPa, and a Poisson's ratio of 0.33. The strain rate effect was incorporated with the Cowper–Symonds model (Equation (4)), with parameters $C = 40$ and $q = 5$.

$$\frac{\sigma_d}{\sigma_0} = 1 + \left(\frac{\dot{\varepsilon}}{C} \right)^{\frac{1}{q}} \tag{4}$$

The fluid domain has dimensions of 1.6 m × 1.6 m × 3.6 m, where the first two coordinates (x, y) are oriented transversely to the structure, with y defining the vertical direction, and the third is defined along the longitudinal axis of the SHG. The free surface elevation is 0.86 m, measured from the bottom extremity of the fluid domain along the y direction. The domain size is sufficient to accurately capture the effects of the primary shock. Flow-out conditions are applied at the boundaries. The discretisation is performed with a graded mesh: cells of 0.05 m are used far from the structure, while around the SHG, the cell size is reduced to 0.025 m (the refined zone has a volume of 0.4 m × 0.7 m × 2.6 m). The presented configuration offers a reasonable compromise between accuracy and computational burden. Regarding the SHG, quadrilateral shell elements were employed, and different sizes, namely, 15 mm, 10 mm, and 5 mm, were tested. Once the discretisation was established based on comparison with experimental data, the same element density had to be adopted while scaling the scenario. This condition guarantees consistent results across different problem scales and has been previously validated in the literature [2,15].

The challenges in CEL simulations arise from the interaction between the Lagrangian and Eulerian meshes, which is typically managed by finite element software through a global coupling algorithm. This procedure is almost automatic and users only need to specify the coupling surface. This approach, however, is inapplicable for complex surfaces, such as for SHGs, due to the numerous compartments and T joints. As an alternative, software packages like Dytran®, which was used in this work, offer a fast coupling algorithm. It requires a closed coupling surface and solely considers Eulerian cells located either outside or inside it. This simplifies the interaction and reduces computational time. In the present scenario, dummy elements were introduced on the upper deck of the SHG to create a closed contact surface and process only the Eulerian cells outside it. This operation disregarded the interaction between air and the internal compartments of

the structure. However, the air inertial effect was negligible and, as common for blast-loaded plate studies [18], the overpressure induced by the UNDEX was the only relevant quantity. Therefore, this strategy did not compromise the accuracy of the results. Dummy elements, while being the most reasonable approach and presumably the same employed by Zhang et al. in the original study [14], yield unsatisfactory results. In fact, these elements are disconnected from the structure and therefore do not follow its deformation. Hence, for significant deformations, the contact surface degenerates, and the results lose accuracy. This issue is experienced only when a structure significantly deviates from its initial configuration and does not affect short-term results, as in Ref. [14].

In this work, to overcome the limitation mentioned above, dummy elements were replaced with structural elements similar to those adopted for the entire SHG. This ensured a closed surface and solved the issues caused by the fast coupling algorithm. Additionally, to replicate the nature of the dummy elements, which lack mass and stiffness, the same material models used for the mild steel were employed by reducing thickness, stiffness, and/or density. The different coupling strategies are illustrated in Figure 4. Although the auxiliary structural elements are even less physically rigorous compared to dummy blocks, they proved effective and allowed for satisfactory results in the numerical simulations. Readers are referred to Section 3 to assess the influence of the auxiliary elements.

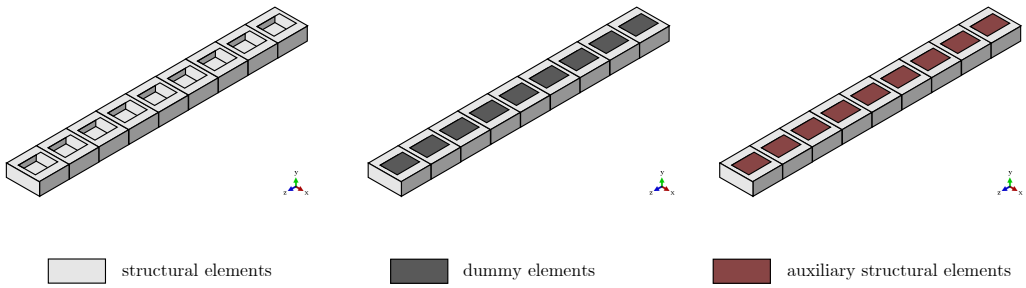

Figure 4. Definition of the Lagrangian elements depending on the coupling strategy: general coupling (left), fast coupling (centre), and fast coupling with replaced dummy elements (right).

2.3. Dimensional Analysis

To create scaled models of prototypes, dimensional analysis is required. This approach aims at identifying governing variables and then expressing their functional relationships in dimensionless terms, thereby reducing their number. Once the non-dimensional relationship is established, scaling factors for each variable are identified to create scaled models. In an SHG, the target variable corresponds to hog distortion δ, expressed as a function of (i) geometric variables, such as length L, height H, width B, thickness h, and cabin longitudinal extension D; (ii) load-related variables, i.e., impulse per unit area I and stand-off distance R; and (iii) material-related variables, i.e., density ρ and static yield strength σ_0 of mild steel. Additionally, time τ is included to characterise hogging motion rather than merely evaluate residual deformation. The functional relation is described in Equation (5).

$$\delta = f(L, H, B, h, D, R, I, \tau, \rho, \sigma_0) \tag{5}$$

The specific impulse I was chosen among several alternatives. In fact, one could consider either the incident/reflected pressure peak or the primary shock energy to characterise the UNDEX blast load. However, the structural behaviour makes the impulse the most logical choice. This is because the global response of the SHG is influenced by the local behaviour of the bottom panel, and it is widely recognised that the deformation of blast-loaded plates is dictated by a dimensionless impulse term [18,19]. Similar considerations have also been made for dams [6].

Furthermore, selecting one of the aforementioned variables is not sufficient to fully characterise a UNDEX blast load. In fact, it is common practice to complement the functional relationship (Equation (5)) with one of the empirical formulas available in Ref. [1]. Equation (6) describes the empirical formula that expresses the impulse, with parameters $K = 5.88$ and $\alpha = 0.89$ for TNT. Although these relations are considered purely empirical formulas, they originate from a dimensionless analysis and assume geometric similarity.

$$I = K\, W^{1/3} \left(\frac{W^{1/3}}{R} \right)^{\alpha} \tag{6}$$

(ρ, σ_0, h) is selected as a set of dimensionally independent variables to determine the non-dimensional relation (Equation (7)). Four dimensionless parameters Π_1, Π_2, Π_3, and Π_4 are identified, where Π_2 describes a generic geometrical ratio among $\frac{L}{h}$, $\frac{H}{h}$, $\frac{B}{h}$, $\frac{D}{h}$, $\frac{R}{h}$. The Π groups associated with the control variables can be combined as long as their number and independence are maintained [20]. Hence, for the sake of simplicity, $\Pi_3' = \Pi_3^2 = \frac{I^2}{\rho \sigma_0 h^2}$ is introduced in the dimensionless equation (Equation (8)).

$$\frac{\delta}{h} = \bar{f}\left(\frac{L}{h}, \frac{H}{h}, \frac{B}{h}, \frac{D}{h}, \frac{R}{h}, \frac{I}{h\sqrt{\rho \sigma_0}}, \frac{\tau}{h}\sqrt{\frac{\sigma_0}{\rho}} \right) \tag{7}$$

$$\Pi_1 = \bar{f}(\Pi_2, \Pi_3, \Pi_4) \Rightarrow \Pi_1 = \tilde{f}\left(\Pi_2, \Pi_3', \Pi_4\right) \tag{8}$$

The creation of scaled models relies on the condition of complete similarity between prototype and model, achieved in accordance with Ref. [20] if the dimensionless parameters remain unchanged. By enforcing the equality of Π groups, the scale factors λ_i (i generic quantity) for the control variables are identified. Each of these defines the ratio between two homologous variables of the model and prototype, and their identification is detailed in Equations (9)–(11).

$$(\Pi_2)_m = (\Pi_2)_p \Rightarrow \frac{(L)_m}{(L)_p} = \frac{(h)_m}{(h)_p} = \lambda \tag{9}$$

$$(\Pi_3)_m = (\Pi_3)_p \Rightarrow \lambda_I^2 = \frac{(I^2)_m}{(I^2)_p} = \frac{(\rho)_m}{(\rho)_p} \cdot \frac{(\sigma_0)_m}{(\sigma_0)_p} \cdot \frac{(h^2)_m}{(h^2)_p} = \lambda_\rho \lambda_{\sigma_0} \lambda^2 \tag{10}$$

$$(\Pi_4)_m = (\Pi_4)_p \Rightarrow \lambda_\tau = \frac{(\tau)_m}{(\tau)_p} = \frac{(\rho^{1/2})_m}{(\rho^{1/2})_p} \cdot \frac{(\sigma_0^{-1/2})_m}{(\sigma_0^{-1/2})_p} \cdot \frac{(h)_m}{(h)_p} = \lambda_\rho^{1/2} \lambda_{\sigma_0}^{-1/2} \lambda \tag{11}$$

By complementing Equations (6) and (10), the scale factor λ_W of the explosive charge mass is identified.

$$\lambda_I = \lambda_\rho^{1/2} \lambda_{\sigma_0}^{1/2} \lambda \Rightarrow \frac{(W^{\frac{1}{3}(1+\alpha)})_m}{(W^{\frac{1}{3}(1+\alpha)})_p} \cdot \frac{(R^\alpha)_p}{(R^\alpha)_m} = \lambda_\rho^{1/2} \lambda_{\sigma_0}^{1/2} \lambda \tag{12}$$

By observing $\frac{(R^\alpha)_p}{(R^\alpha)_m} = \lambda^{-\alpha}$ and rearranging the term of Equation (12), the functional expression of λ_W arises, as described in Equation (13).

$$\lambda_W^{1/3} = \lambda_\rho^{\frac{1}{2(1+\alpha)}} \lambda_{\sigma_0}^{\frac{1}{2(1+\alpha)}} \lambda \tag{13}$$

Equations (10), (11), and (13) define a system of 3 algebraic equations that can be solved by choosing a scale factor λ. Furthermore, by selecting the same material for model and prototype, i.e., imposing the invariance of density and static yield strength, a trivial solution is obtained: the entire set of control variables is scaled solely based on geometrical similarity, represented by the scale factor λ. In particular, by enforcing the conditions $\lambda_\rho = 1$ and $\lambda_{\sigma_0} = 1$, Equation (13) becomes Equation (14), which corresponds to the cube root scaling

law independently formulated by Hopkinson [21] and Cranz [22] and commonly employed to scale explosions in air and water.

$$\lambda_W^{1/3} = \lambda \tag{14}$$

By raising Equation (14) to the power of 3/2, the impact factor introduced by Yao et al. [5] is obtained as shown in Equation (15). The thickness h appears instead of the stand-off distance R due to the different choice of the variable triplet for the non-dimensional analysis.

$$\lambda_W^{1/2} = \lambda^{3/2} \Rightarrow \left(\frac{\sqrt{W}}{h^{3/2}}\right)_m = \left(\frac{\sqrt{W}}{h^{3/2}}\right)_p \tag{15}$$

The impact factor thus originates from the Hopkinson–Cranz law and depends solely on geometrical similarity. In conclusion, the procedure formalised in this section, along with the impact factor described in Equation (15), derives from the cube root scale. This result once again highlights the objective of this work, i.e., a study of the applicability of a similarity law based solely on static–geometric considerations to an SHG.

3. Results

Three subsections present the results: the first discusses the applicability of the coupling strategy based on auxiliary structural elements, the second presents the validation of the numerical prototype and the selection of the element size for the Lagrangian mesh, and the third addresses the creation of scaled models through numerical simulations.

3.1. Coupling Procedure

Figure 5 shows the hogging motion of the full-scale SHG using different coupling approaches.

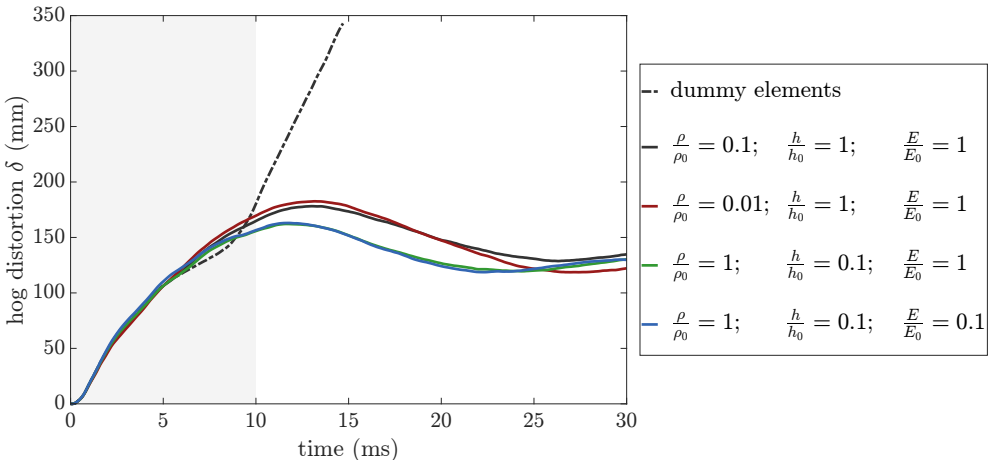

Figure 5. Hogging motion for different coupling strategies and various choices of auxiliary structural element parameters.

These results were obtained using Lagrangian elements with a uniform size of 15 mm. Specifically, the fast coupling algorithm based on dummy elements yielded unsatisfactory results. For durations greater than 10 ms, i.e., the simulated time in the original work [14], the curve significantly diverged from the expected parabolic trend. Consequently, auxiliary structural elements were introduced as replacements for the dummy elements, resolving the coupling issues without significantly altering the overall behaviour. To demonstrate this, the hogging motions obtained by varying the density, thickness, and/or stiffness (Young's modulus E) of the auxiliary elements are shown. A density or thickness of 10% compared to the nominal value resulted in a 1.6% increase in the SHG's mass, which is

considered negligible. The curves maintained the same overall trend with small variations in the peak, regardless of the selected parameters. Therefore, the coupling procedure was deemed satisfactory, and the results presented in the following sections were computed leveraging auxiliary structural elements.

3.2. Numerical Prototype Validation

Figure 6 illustrates the hogging motion of the SHG caused by the primary shock for various Lagrangian element sizes. These curves were obtained using the auxiliary structural elements. The numerical results were compared to the raw experimental data and the corresponding quadratic fitting. The raw data were extracted from Ref. [14], while the quadratic fitting was slightly modified as the original work lacked specific details on how the first data point, corresponding to the beginning of the transient, was derived. Therefore, the first experimental point was excluded, and the fitting was performed on data expressed in (mm, ms) instead of (m, s), leading to Equation (16). This improved the quality of the approximation, increasing the coefficient of determination from 0.996 to 0.999, and provided a fairer comparison with the numerical results. As an example, Figure 7 shows the deformed configuration of the SHG discretised with 10 mm elements at maximum hogging. The plastic hinge at the midpoint and the rigid behaviour of the side surfaces were accurately captured. Figure 8 provides a zoom-in view of the central cabin of the SHG at the same time instant to show the local deformation of the lower plate. The global deformation of the structure aligned with the experiments, although the local behaviour of the two side plates was not perfectly replicated. A similar local deformed shape was obtained in the original work numerically; hence, the model is deemed accurate.

$$\delta(t) = -0.653 \cdot t^2 + 32.534 \cdot t - 40.948 \tag{16}$$

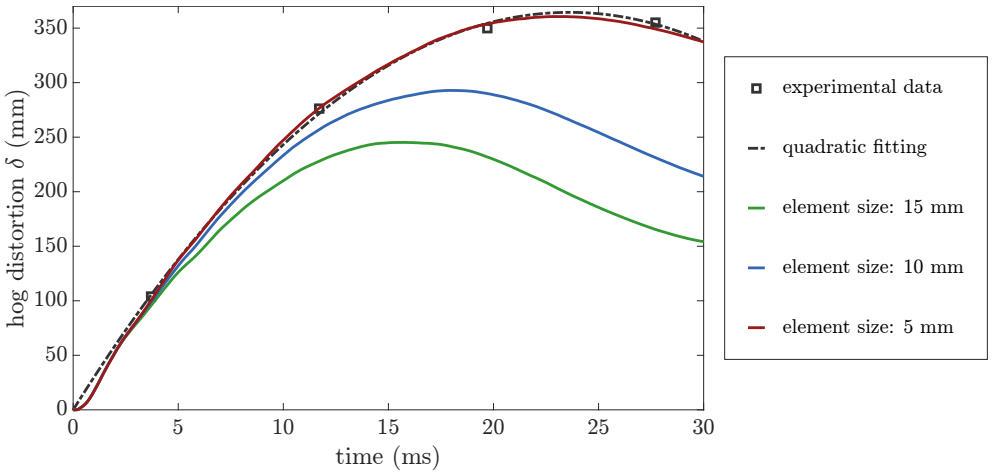

Figure 6. Comparison between numerically computed and experimental hog distortion with variable Lagrangian element size (both structural and auxiliary).

3.3. Scaled SHG Models

The scaled numerical models of the prototype were obtained using a Lagrangian mesh with a fixed element density, which was defined by the original mesh with 15 mm elements. This choice reduced the computational time by approximately one order of magnitude, and, despite the numerical results slightly differing from the experimental behaviour, it did not affect the scaling procedure. Figure 9 shows the results in dimensionless terms for six different values of the geometric scaling factor λ. $\lambda = 1$ defines the numerical prototype, and the hogging motion curve coincides, after non-dimensionalisation, with the one presented in Figure 6, considering 15 mm finite elements. The remaining curves were obtained from models scaled down relative to the prototype. The hogging motion of

the scaled models significantly diverged from the prototype trend for non-dimensional times ($\tau \cdot h^{-1} \cdot \sigma_0^{1/2} \cdot \rho^{-1/2}$) greater than approximately 120. As the scaling factor increased, the hogging of the structure progressively decreased, showing similar behaviour for lower scaling factors.

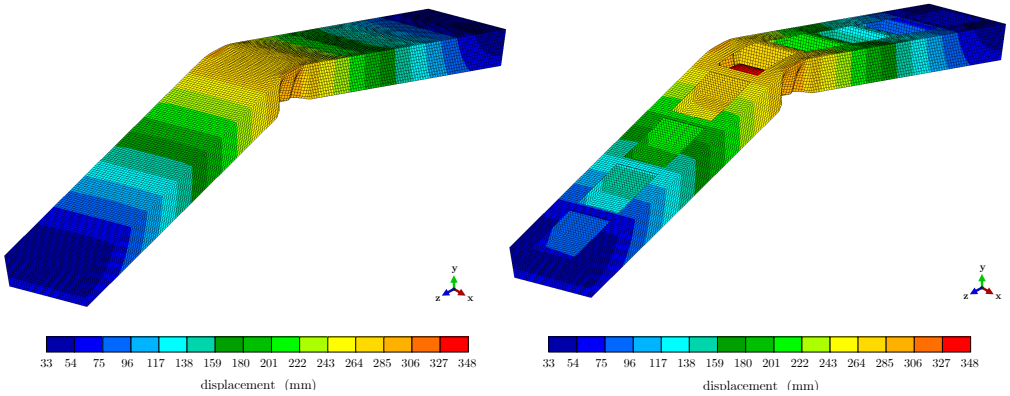

Figure 7. Displacement contour plot at maximum hogging (τ = 17.5 ms) for the SHG prototype discretised with a 10 mm mesh: structural and auxiliary elements (left); only structural elements (right).

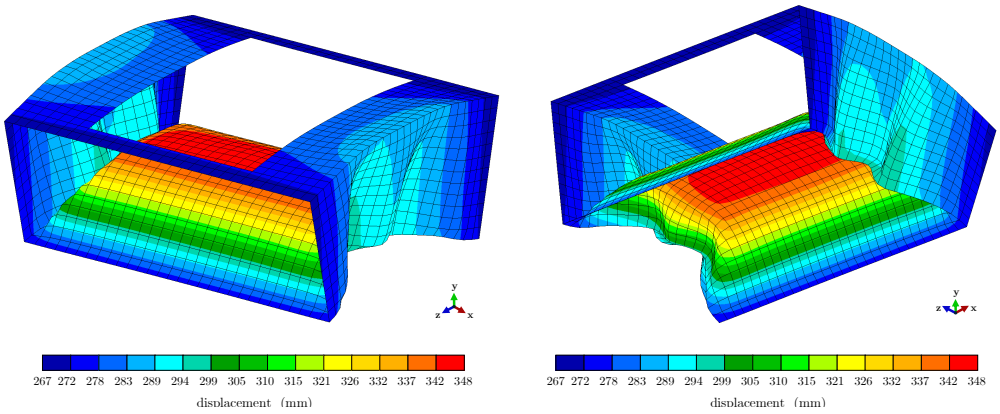

Figure 8. Displacement contour plot at maximum hogging (τ = 17.5 ms) for the central cabin of the SHG prototype discretised with a 10 mm mesh: top view (left) and bottom view (right).

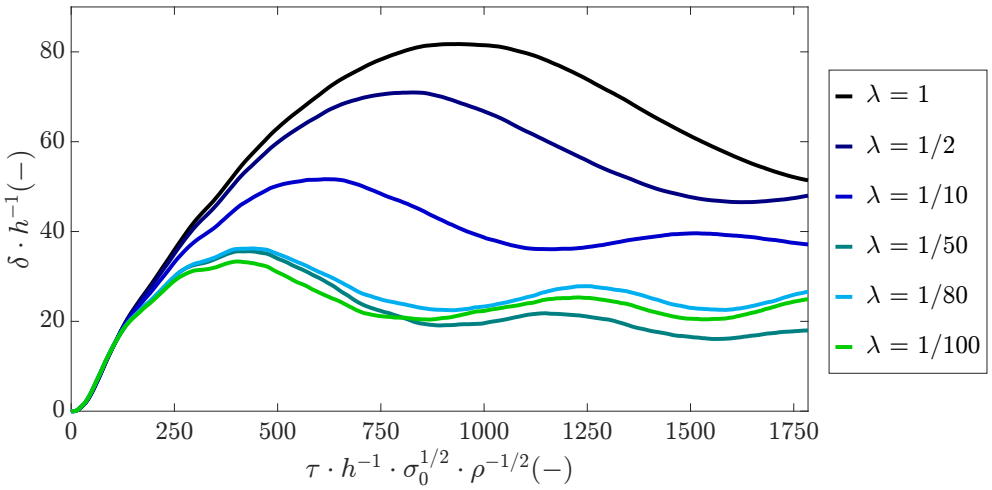

Figure 9. Hog motion comparison among prototype and scaled models; numerical analysis conducted with 15 mm Lagrangian mesh.

4. Discussion

Experimentally, the hogging motion of the SHG due to the primary shock is described in time by a quadratic fitting (Equation (16)). Therefore, even before validating the numerical model, the accuracy of the fluid–structure coupling algorithm was assessed through a qualitative investigation of the hog distortion, motivating the discussion in Section 3.1. From Figure 5, one can deduce that the complexity of the coupling structure does not permit the satisfactory usage of conventional coupling algorithms, due to the presence of bulkheads and T joints. In fact, when the lower plate of the SHG surpasses the stationary dummy elements, the coupling surface overturns. Consequently, the expanding gas bubble fills with atmospheric air carried under the structure due to the overturning of the contact surface. As an immediate result, the bubble collapses and produces a severe reloading of the SHG, justifying the diverging curve in Figure 5 (dashed curve). Auxiliary structural elements overcome this issue. It is important to note that, ideally, the density of these elements should tend toward zero to avoid altering the structural behaviour. However, this would compromise the computational time, as the time step depends on the natural frequency of the structural elements and, ultimately, on the material density. All results shown in Sections 3.2 and 3.3 were obtained by choosing a ratio $\rho/\rho_0 = 0.1$ to avoid burdening the calculations.

The scaling procedure based solely on the geometric factor does not yield satisfactory results. As the structure is scaled, it exhibits increasingly rigid behaviour. This is due to the strain rate effect $(\dot{\varepsilon})$, which was not considered. Equation (17) introduces the non-dimensional group for the strain rate.

$$\Pi_5 = \dot{\varepsilon}\sqrt{\frac{\rho}{\sigma_0}}h \tag{17}$$

The strain rate scale factor is obtained as shown in Equation (18).

$$(\Pi_5)_m = (\Pi_5)_p \Rightarrow \lambda_{\dot{\varepsilon}} = \frac{(\sigma_0^{1/2})_m}{(\sigma_0^{1/2})_p} \cdot \frac{(\rho^{-1/2})_m}{(\rho^{-1/2})_p} \cdot \frac{(h^{-1})_m}{(h^{-1})_p} = \lambda_{\sigma_0}^{1/2}\lambda_{\rho}^{-1/2}\lambda^{-1} \tag{18}$$

This expression shows that, with static yield strength and density kept constant, the strain rate is inversely proportional to the geometric scale factor. This is confirmed by the numerical results shown in Figure 10, which focus on the central cabin and two different scale factors $\lambda = 1$ and $\lambda = 100$. As a result, the dynamic stress varies as predicted by Equation (4), leading to a stiffer response in the scaled models. Similar results have been reported in the literature concerning impact problems [23].

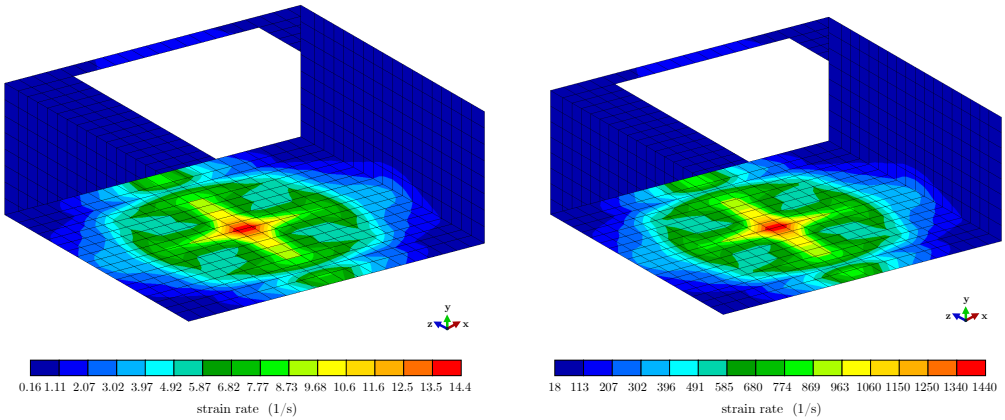

Figure 10. Comparison of the strain rate colour plot at the non-dimensional time $\tau = 60$ for the numerical prototype (left) and the scaled model with $\lambda = 100$ (right).

Furthermore, the trends in Figure 9 show no significant differences in the hogging motion shortly after the impact. This suggests that the scaling procedure can be applied to the early response of the SHG, indicating that it is not significantly affected by the strain rate. This also clarifies the findings in Ref. [5], where SHG scaling was performed without specifying the time instants at which it was applied. To further demonstrate this interpretation and the dominant role of the strain rate, an additional simulation was carried out for both the prototype and the scaled model with $\lambda = 100$, this time removing the strain-rate dependence of the yield strength. The resulting hogging behaviour is shown in Figure 11, alongside the previous trends. The absence of strain-rate effects leads to a much more pronounced hog distortion, but, more importantly, the early response remains similar to the strain-rate-dependent models. This supports the validity of the scaling procedure when limited to the initial phase of the structural response.

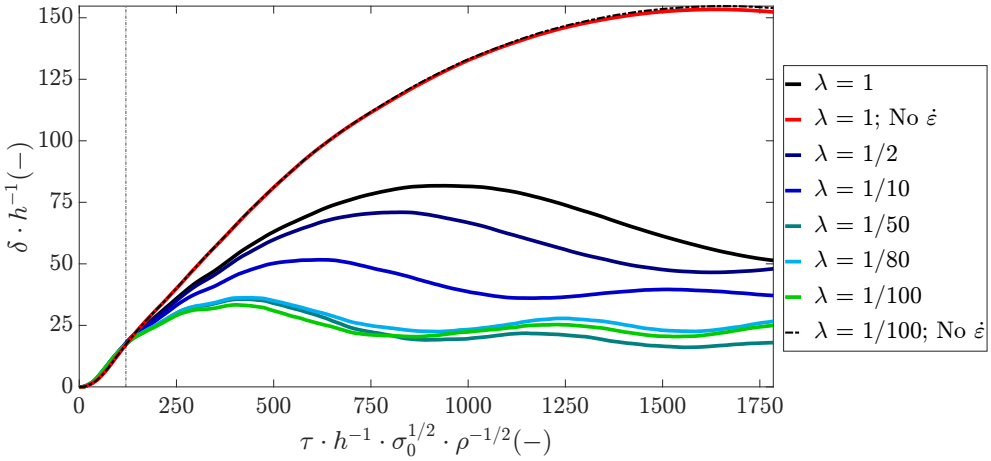

Figure 11. Hogging motion for scaled SHG models with and without incorporating the influence of the strain rate on the yield strength.

To further investigate the different hogging motions of the scaled models due to the strain-rate effect, two quantities can be considered: kinetic energy E_k and distortional energy E_d (i.e., the energy of deformation). The trends in these two quantities are shown in Figures 12 and 13, considering their dimensionless expressions. Valuable insights can be drawn by comparing the behaviour of the energy terms across the different scaled models with that of the prototype ($\lambda = 1$). The early response is similar, and, consequently, the energy terms follow comparable trends. When the hog distortion curves begin to diverge ($\tau = 120$, highlighted by the dashed line), the kinetic energy of the scaled models tends to increase compared to the prototype, while the distortional energy decreases. This indicates that the scaled structures undergo less deformation while maintaining higher velocities compared to the prototype. The increased velocity can therefore only be attributed to the rigid motion of the scaled SHGs, as demonstrated in Figure 14.

The latter shows the rigid motion w_0 of the structure as the scaling factor varies, confirming this interpretation. Furthermore, it becomes evident that the natural progression of this work is to establish a scaling procedure that, while not maintaining complete similarity, replicates the behaviour of the SHG prototype beyond the early response phase. This outcome can only be achieved by compensating for strain-rate effects.

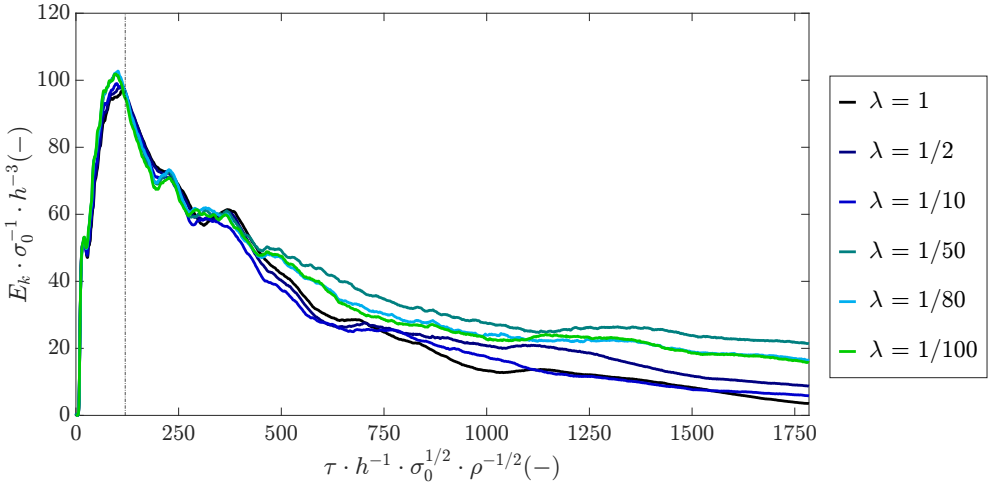

Figure 12. Kinetic energy trend for SHG prototype and scale models.

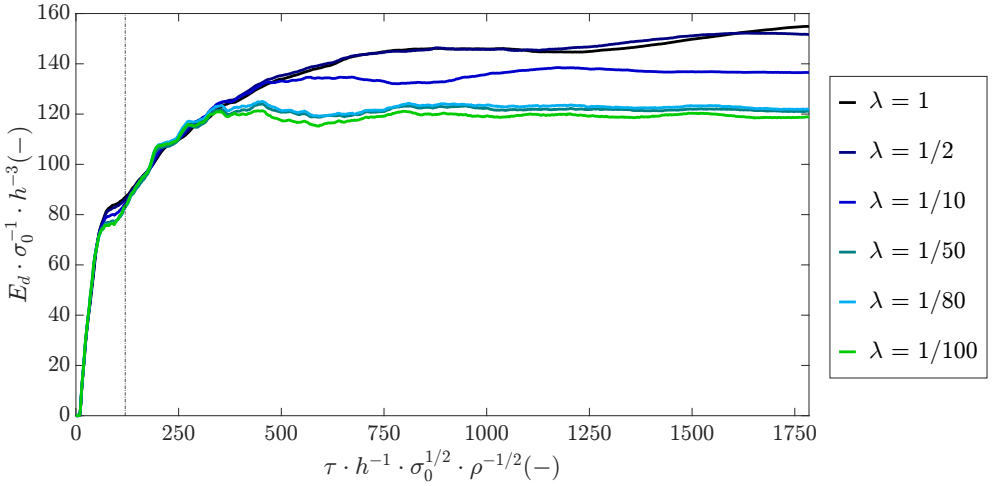

Figure 13. Distortional energy trend for SHG prototype and scale models.

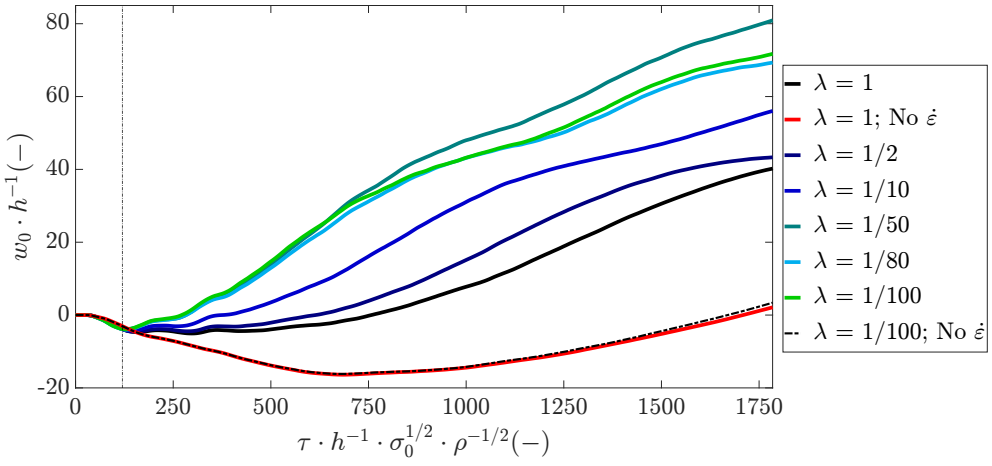

Figure 14. Rigid motion for SHG prototype and scale models.

5. Conclusions

In this study, a practical numerical modelling strategy for fluid–structure interaction was introduced, addressing configurations where traditional methods are unsatisfactory. In particular, artificial structural elements were introduced to establish the connection between the Eulerian and Lagrangian meshes, solving the experienced coupling issues. This approach was then leveraged to develop a high-fidelity prototype of a simplified hull

girder subjected to a shock induced by an underwater explosion, which was validated against experimental data from the literature. By employing the validated method and the outlined scenario, the possibility of creating scaled models for laboratory testing based solely on static–geometric considerations, as suggested in the literature, was explored. The numerical findings indicated that these scaled models accurately replicated the behaviour of the prototype only during the early response phase. To achieve consistency throughout the entire response, it is essential to recognise and account for the critical role of strain-rate effects.

Author Contributions: Conceptualisation, G.M., L.L., and A.M.; methodology, G.M. and L.L.; software, G.M.; validation, G.M.; formal analysis, G.M. and L.L.; investigation, G.M. and L.L.; resources, G.M.; data curation, G.M.; writing—original draft preparation, G.M.; writing—review and editing, G.M., L.L., and A.M.; visualisation, G.M.; supervision, A.M.; project administration, A.M.; funding acquisition, A.M. and M.G. All authors have read and agreed to the published version of the manuscript.

Funding: This research received no external funding.

Institutional Review Board Statement: Not applicable.

Informed Consent Statement: Not applicable.

Data Availability Statement: Data are contained within this article.

Conflicts of Interest: The authors declare no conflicts of interest.

Abbreviations

The following abbreviations are used in this manuscript:

FSI	Fluid–structure interaction
SHG	Simplified hull girder
UNDEX	Underwater explosion

Nomenclature

a_1, A_1, A_2, R_1, R_2, γ, ω	Equation of state parameters
B	SHG width
b	Larger deck stringer width
C, q	Copwer–Symonds model parameters
D	SHG cabin length
E	Young's modulus
E_d	Distortional energy
E_k	Kinetic energy
e	Internal energy per unit mass
f, $\bar{f}$, $\tilde{f}$	Generic relations
H	SHG height
h	Thickness
I	Impulse per unit area
L	SHG length
l	Smaller deck stringer length
p	Pressure
p_0	Reference pressure
R	Explosive charge stand-off distance
W	Explosive charge mass

w_0	Rigid motion
Z	Scaled distance
α, K	Empirical parameters
δ	Hog distortion
$\dot{\varepsilon}$	Strain rate
λ	Geometrical scale factor
λ_i	Scale factor for quantity i
Π	Dimensionless number
ρ	Density
ρ_0	Reference density
σ_0	Static yield strength
σ_d	Dynamic yield strength
τ	Time

References

1. Cole, R. *Underwater Explosions*; Dover Publications: Mineola, NY, USA, 1948.
2. Noam, T.; Dolinski, M.; Rittel, D. Scaling dynamic failure: A numerical study. *Int. J. Impact Eng.* **2014**, *69*, 69–79. [CrossRef]
3. Kong, X.; Li, X.; Zheng, C.; Liu, F.; Wu, W.-g. Similarity considerations for scale-down model versus prototype on impact response of plates under blast loads. *Int. J. Impact Eng.* **2017**, *101*, 32–41. [CrossRef]
4. Fu, T.; Zhang, M.; Zheng, Q.; Zhou, D.; Sun, X.; Wang, X. Scaling the response of armor steel subjected to blast loading. *Int. J. Impact Eng.* **2021**, *153*, 103863. [CrossRef]
5. Yao, X.; Zhao, K.; Shi, D. Study on the effectiveness of impact factor in underwater explosion model test. *Int. J. Impact Eng.* **2024**, *185*, 104839. [CrossRef]
6. Huang, X.; Kong, X.; Hu, J.; Fang, Q. Scaling the failure of concrete gravity dam subjected to underwater explosion—Part I: Suggestion of a dimensionless number. *Ocean Eng.* **2023**, *277*, 114316. [CrossRef]
7. Huang, X.; Kong, X.; Hu, J.; Fang, Q. Scaling the failure of concrete gravity dam subjected to underwater explosion—Part II: Correction method to consider the strain-rate effect. *Ocean Eng.* **2023**, *281*, 114728. [CrossRef]
8. Ge, S.; Zu-yu, C.; Yuan, L.; Ming-shou, Z.; Jian-yu, W. Experimental and numerical investigation of the centrifugal model for underwater explosion shock wave and bubble pulsation. *Ocean Eng.* **2017**, *142*, 523–531. [CrossRef]
9. He, Z.; Chen, Z.; Jiang, Y.; Cao, X.; Zhao, T.; Li, Y. Effects of the standoff distance on hull structure damage subjected to near-field underwater explosion. *Mar. Struct.* **2020**, *74*, 102839. [CrossRef]
10. Li, X.; Liang, M.; Tian, Z.; Zhou, M. Dynamic response and cumulative damage mechanism of simplified hull girders under repeated underwater explosions. *Thin-Walled Struct.* **2024**, *196*, 111554. [CrossRef]
11. Li, H.; Zhu, Y.; Liu, K.; Zou, H.; Chen, X.; Wang, H. Experimental study of the coupled damage characteristics of a large-scale hull girder subjected to an underwater near-field explosion. *Thin-Walled Struct.* **2024**, *196*, 111547. [CrossRef]
12. Zhang, W.; Gong, Y.; Du, Z. Study on structural damage mechanisms and defence of rectangular closed-section simplified hull girders with thinner plates under near-field underwater explosions. *Ocean Eng.* **2024**, *294*, 116800. [CrossRef]
13. Li, H.; Zheng, X.; Zhang, C.; Mei, Z.; Bai, X.; Liu, K. Sagging damage characteristics of hull girder with trapezoidal cross-section subjected to near-field underwater explosion. *Def. Technol.* **2023**, *21*, 1–13. [CrossRef]
14. Zhang, Z.; Wang, Y.; Zhao, H.; Qian, H.; Mou, J. An experimental study on the dynamic response of a hull girder subjected to near field underwater explosion. *Mar. Struct.* **2015**, *44*, 43–60. [CrossRef]
15. Huang, X.; Kong, X.; Hu, J.; Fang, Q. Scaling the failure of concrete gravity dam subjected to underwater explosion shock loading. *Ocean Eng.* **2022**, *261*, 112176. [CrossRef]
16. Lee, E.L.; Hornig, H.C.; Kury, J.W. Adiabatic Expansion Of High Explosive Detonation Products. 1968. Available online: https://www.osti.gov/servlets/purl/4783904/ (accessed on 1 July 2024).
17. Century Dynamics. *AUTODYN Theory Manual, Revision 4.3*; Century Dynamics: Fort Worth, TX, USA, 2005.
18. Ramajeyathilagam, K.; Vendhan, C. Deformation and rupture of thin rectangular plates subjected to underwater shock. *Int. J. Impact Eng.* **2004**, *30*, 699–719. [CrossRef]
19. Chung Kim Yuen, S.; Nurick, G.; Langdon, G.; Iyer, Y. Deformation of thin plates subjected to impulsive load: Part III—An update 25 years on. *Int. J. Impact Eng.* **2017**, *107*, 108–117. [CrossRef]
20. Buckingham, E. On Physically Similar Systems; Illustrations of the Use of Dimensional Equations. *Phys. Rev.* **1914**, *4*, 345–376. [CrossRef]
21. Hopkinson, B. *British Ordnance Board Minutes*; Technical Report 13565; British Ordnance Office: London, UK, 1915.

22. Cranz, K.J.; v. Eberhard, O.; Becker, K.E. *Lehrbuch der Ballistik. Ergänzungen zum Band II*; J. Springer: Berlin/Heidelberg, Germany, 1926.
23. Oshiro, R.; Alves, M. Predicting the behaviour of structures under impact loads using geometrically distorted scaled models. *J. Mech. Phys. Solids* **2012**, *60*, 1330–1349. [CrossRef]